arXiv:1403.6072v1 [cond-mat.mtrl-sci] 24 Mar 2014

Visualizing Skin Effects in Conductors with MRI: ^{7}Li MRI Experiments and Calculations

Andrew J. Ilott[a], S. Chandrashekar[b], Andreas Klöckner[c], Hee Jung Chang[d], Nicole M. Trease[d], Clare P. Grey[d,e], Leslie Greengard[f], Alexej Jerschow[a,*]

[a]*Department of Chemistry, New York University, 100 Washington Square East, New York, NY 10003, USA.*
[b]*National High Magnetic Field Laboratory and Florida State University, 1800 E. Paul Dirac Drive, Tallahassee, FL 32310, USA.*
[c]*Department of Computer Science, University of Illinois at Urbana-Champaign, Urbana, IL, 61801, USA.*
[d]*Department of Chemistry, Stony Brook University, Stony Brook, NY 11794, USA.*
[e]*Department of Chemistry, University of Cambridge, Lensfield Road, Cambridge CB2 1EW, UK.*
[f]*Courant Institute of Mathematical Sciences, New York University, New York, NY 10012, USA.*

Abstract

While experiments on metals have been performed since the early days of NMR (and DNP), the use of bulk metal is normally avoided. Instead, often powders have been used in combination with low fields, so that skin depth effects could be neglected. Another complicating factor of acquiring NMR spectra or MRI images of bulk metal is the strong signal dependence on the orientation between the sample and the radio frequency (RF) coil, leading to non-intuitive image distortions and inaccurate quantification. Such factors are particularly important for NMR and MRI of batteries and other electrochemical devices. Here, we show results from a systematic study combining RF field calculations with experimental MRI of ^{7}Li metal to visualize skin depth effects directly and to analyze the RF field orientation effect on MRI of bulk metal. It is shown that a certain degree of selectivity can be achieved for particular faces of the metal, simply based on the orientation of the sample. By combining RF field calculations with bulk magnetic susceptibility calculations accurate NMR spectra can be obtained from first principles. Such analyses will become valuable in many applications involving battery systems, but also metals, in general.

Keywords: Magnetic Resonance Imaging, Lithium batteries, RF field calculations, Susceptibility effects, Skin effect

1. Introduction

It is well known that electromagnetic fields decay upon entering conducting regions [1]. For good conductors, the fields can be shown to decay exponentially with a characteristic distance,

*Corresponding author
Email address: alexej.jerschow@nyu.edu (Alexej Jerschow)

δ, referred to as the skin depth,

$$\delta = \sqrt{\frac{\rho}{\pi\mu_0\mu_r\nu}}, \tag{1}$$

where ν is the frequency of the field, μ_0 the permeability of free space, μ_r the relative permeability of the conductor and ρ its resistivity. At typical NMR frequencies (70–300 MHz for nuclei other than protons) δ is of the order of 10s of μm for good metal conductors ($\rho \approx 10^{-8}$ Ωm). The skin depth hence determines the limited region within which NMR-active nuclei can be probed in a conducting sample.

In previous NMR studies of metals, skin effects have been typically avoided by using low magnetic fields and powdered samples to maximize sensitivity. This approach was appropriate for most early studies, where there was interest in measuring the Knight shifts and relaxation times of metal nuclei in order to probe the hyperfine interactions and gain insight into the electronic structure of metals [2, 3, 4, 5, 6]. Indeed, there have been successful studies on powdered metals, both pure [4, 7, 8, 9, 10, 11] and alloyed [10, 12, 13, 14, 15]. Powdered metal conductors were also amongst the first samples proposed for dynamic nuclear polarization (DNP) transfer experiments [16].

Aside from the skin depth effects, which restrict sensitivity by limiting the effective sample size, samples containing bulk conducting metals are further afflicted by artifacts due to their interactions with the static and the RF magnetic fields used in MR experiments. Interactions with the static field can introduce large local $\boldsymbol{B}_0$ field inhomogeneities in the proximity of arbitrarily shaped, bulk metal that are a consequence of the typically large magnetic susceptibilities of many metals. The extent of these artifacts depends on the shape of the metal object and its relative orientation with respect to the external, $\boldsymbol{B}_0$ field. The second effect is due to the conducting properties of the metal, which lead to the induction of surface currents when the sample is irradiated with an oscillating RF field [17]. The induced currents modify the effect of the RF field at the surface of the metal and in the immediate vicinity of it, impacting the excitation and detection of the nuclear spins in these regions. The RF effect also depends on the sample shape and its orientation with respect to the applied RF, as both of these factors dictate the form of the induced current.

Traditionally, the above problems have been most strongly associated with reports of artifacts in clinical MRI scanning originating from the presence of metallic implants [18]. Recently, these effects have also become pertinent problems in the development of NMR and MRI techniques for the *in situ* study of electrochemical devices. Here, the use of conducting components is clearly a requirement. Indeed, *in situ* NMR [19, 20] and MRI [21, 22] of functioning Li-metal batteries have given great insight into properties of the electrolyte and the metal electrodes during the charge cycles in such systems. The strong susceptibility effects associated with the regions surrounding the Li-metal have even proven to be advantageous for such studies, as they give rise to distinct and characteristic chemical shifts for surface microstructures and dendrites [19, 21]. As a result, chemical shift images (CSIs) not only revealed the location of such entities, but also

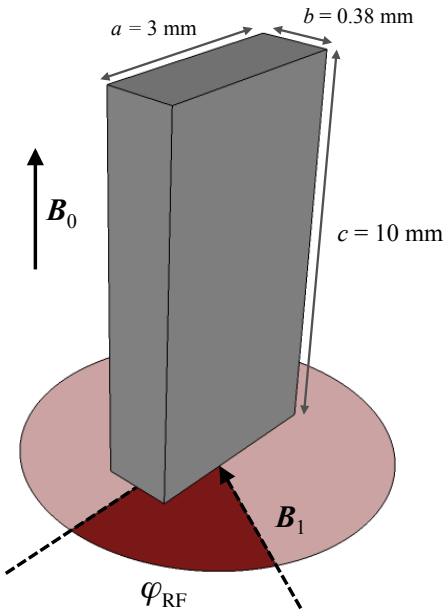

Figure 1: Schematic of the cell used in the MRI experiments and calculations to represent the lithium metal electrode. The c axis of the rectangular strip is aligned along the external magnetic field, $\boldsymbol{B}_0$. The angle ϕ_{RF} specifies the relative orientation between the plane of the ac metal surface with the magnetic field component of the RF field.

some of their characteristics. In previous studies, qualitative rules have been followed to align the main face of the (square) conducting metal electrodes with the RF field direction in order to minimize RF field inhomogeneities, but the RF field dependence on orientation and shape were not known [21, 23, 24].

In this work, we combine RF field and bulk magnetic susceptibility calculations with experimental NMR and MRI results to clarify the role of the RF-field orientation, skin effects, and susceptibility shifts in determining the appearance of spectra and images of bulk metals and samples that contain them. The experiments and calculations are performed on ^{7}Li metal, a moderately good conductor, but also a highly relevant material in battery applications where the insights provided should be of particular value. It is shown that all of the above effects can be accounted for explicitly, with an excellent agreement between calculation and experiment. Furthermore, the calculation methods are robust and easily extended to more complicated systems. Insights from these should prove beneficial for future studies and aid in the development of promising novel techniques for bulk metal NMR and MRI.

2. Methods

2.1. Magnetic resonance imaging.

The sample consisted of a ~10 x 3 x 0.38 mm strip of ^{7}Li metal (Aldrich, 99.9%) within a standard 5 mm o.d. NMR tube. Strips of glass microfiber separator were placed on either side of the metal strip to center it in the tube and to secure it tightly in place during the experiments. The sample was assembled and sealed inside an argon glove box.

All MRI and NMR experiments were performed on a Bruker Ultrashield 9.4 T Avance I spectrometer containing a Bruker Micro2.5 gradient assembly and operating at 155.51 MHz for ^{7}Li. A wide band HR-50 probe (Cryomagnet Systems Inc., Indianapolis) equipped with a 5 mm saddle coil was used to collect all of the images. In this setup, the sample is free to rotate in the probe and the probe free to rotate inside the gradient stack, allowing the angle between the sample and RF field direction, ϕ_{RF}, and between the sample and principal gradient directions, ϕ_{Gx}, to be set independently.

The images were acquired without slice selection using a spin echo pulse sequence with 64 phase encoding steps incrementing the gradient strength between ±38.2 G cm^{-1} and applied for 750 μs with a 75 μs ramp time, giving a 6.0 mm field of view (FOV) and nominal 94 μm resolution. A 45.3 G cm^{-1} frequency encoding gradient was used during acquisition with a 30 kHz spectral width, giving a FOV and nominal resolution of 4.0 mm and 31 μm. For each required orientation, ϕ_{RF}, the gradient orientation was kept constant, $\theta_{Gx} = 0°$, so that the phase direction was parallel to the face of the metal strip, and the frequency encoded direction perpendicular to it. The total echo time, TE, and repetition time, TR, were 1.1 ms and 100 ms, respectively. Pulses corresponding to a power of 5 kHz were used for excitation and refocusing. This same pulse power was also used to acquire a 1D NMR spectrum at each orientation. Chemical shifts were referenced to 1 M LiCl at 0.0 ppm.

2.2. Numerical Simulations.

2.2.1. Calculation of Electromagnetic Fields.

For the numerical simulations, the electrodes were modeled as perfect electric conductors scattering an incident plane wave with wave number $k = 100$ cm^{-1}, corresponding to an excitation at a wave length of $\lambda = 2\pi/k \approx 62$ cm. The incident wave was taken to be propagating along the x axis and linearly polarized along the z axis.

The non-dimensionalized, time-harmonic, linear, isotropic Maxwell's equations [1]

$$\begin{aligned} \nabla \times \boldsymbol{H} + ik\boldsymbol{E} &= 0 \\ \nabla \times \boldsymbol{E} - ik\boldsymbol{H} &= 0 \\ \nabla \cdot \boldsymbol{E} &= 0 \\ \nabla \cdot \boldsymbol{H} &= 0 \end{aligned}$$

were used with perfect electric conductor (PEC) boundary conditions

$$\boldsymbol{n} \times \boldsymbol{E}^{\text{tot}} = 0, \quad \boldsymbol{n} \cdot \boldsymbol{H}^{\text{tot}} = 0 \qquad \text{on the metal surface} \tag{2}$$

where $\boldsymbol{n}$ is the unit normal to the metal surface.

These equations were then solved for the scattered field

$$\boldsymbol{E} = \boldsymbol{E}^{\text{tot}} - \boldsymbol{E}^{\text{inc}}, \qquad \boldsymbol{H} = \boldsymbol{H}^{\text{tot}} - \boldsymbol{H}^{\text{inc}}.$$

$\boldsymbol{E}^{\text{inc}}$ and $\boldsymbol{H}^{\text{inc}}$ here are defined as the incident plane wave described above.

To obtain a numerical solution, the problem was recast as a variant of the magnetic field integral equation [25] with surface charge and current densities ρ and $\boldsymbol{J}$ as unknowns [26, 27]

$$\boldsymbol{J}/2 - \boldsymbol{n} \times (\nabla \times S_k \boldsymbol{J}) = \boldsymbol{n} \times \boldsymbol{H}^{\text{inc}} \tag{3}$$

$$\rho/2 + \hat{n} \cdot \nabla S_k \rho = \boldsymbol{n} \cdot \boldsymbol{E}^{\text{inc}} + ik(\boldsymbol{n} \cdot S_k \boldsymbol{J}), \tag{4}$$

where S_k is the single layer *scalar* potential operator for the Helmholtz equation [28]

$$S_k \rho(\mathbf{x}) := \frac{1}{4\pi} \int_\Gamma \frac{e^{ik|\mathbf{x}-\mathbf{x}'|}}{|\mathbf{x}-\mathbf{x}'|} \rho(\mathbf{x}') ds_{x'} \,, \tag{5}$$

and where $\mathbf{x}$ and $\mathbf{y}$ are coordinates in $\mathbb{R}^3$.

Note that the surface current density is a tangential vector field, following from $\boldsymbol{n} \times \boldsymbol{H}^{\text{inc}}$, so equations (3) and (4) form a (square) system of Fredholm boundary integral equations of the second kind [28].

Equations (3) and (4) were solved iteratively using GMRES [29], and values for $\boldsymbol{E}$ and $\boldsymbol{H}$ were recovered at all target locations from $\boldsymbol{J}$ and ρ according to the representations

$$\boldsymbol{E}(\mathbf{x}) = ikS_k \boldsymbol{J}(\mathbf{x}) - \nabla S_k \rho(\mathbf{x}),$$
$$\boldsymbol{H}(\mathbf{x}) = \nabla \times S_k \boldsymbol{J}(\mathbf{x}).$$

$\boldsymbol{J}$ and ρ were discretized as piecewise constants on a triangular grid tessellating the surface of the electrode. The integrals in the layer potentials on each triangle were computed by "singularity subtraction": analytically for the static kernel $1/|\mathbf{x}-\mathbf{y}|$ and by high order Gaussian quadrature for the smoother remainder $(e^{ik|\mathbf{x}-\mathbf{y}|} - 1)/|\mathbf{x}-\mathbf{y}|$. The calculation was accelerated by making use of the low frequency fast multipole method (FMM), described in [30]. FMM-accelerated integral equation methods permit the solution of electromagnetic scattering problems in $O(N \log N)$ time, where N denotes the number of degrees of freedom in the discretization of the scatterer. Unlike finite difference or finite element methods, integral equation methods do not require a discretization of the domain itself and impose radiation conditions at infinity by construction. We made use of the open-source `FMMLIB3D` library [31].

Triangular surface meshes for the electrodes were generated using the Gmsh mesh generator [32]. Care was taken to devote a substantial amount of resolution to the singularities of charge

and current densities along edges and corners. Characteristic lengths for the mesh were set to $3.5 \cdot 10^{-7}$ m at corners and to $7 \cdot 10^{-6}$ m elsewhere.

Only the x and y components of the $\boldsymbol{H}^{\text{tot}}$ RF field are perpendicular to $\boldsymbol{B}_0$ and hence excite the precessing nuclear spins. The nuclear magnetization nutates at a rate that is proportional to the strength of the RF field at each of the q triangles in the mesh,

$$\omega_q = \frac{|H_q^{\text{tot}}(x) + H_q^{\text{tot}}(y)|}{2\pi}. \tag{6}$$

The variation of ω_q leads directly to a variation in the detected signal at each triangle,

$$F_q \propto \omega_q \sin\left(\omega_q \tau\right), \tag{7}$$

using the principle of reciprocity [33]. The effective pulse length, τ, is chosen such that $\omega_q \tau = \pi/2$ when $|H_q^{\text{tot}}(x) + H_q^{\text{tot}}(y)| = 1$. This procedure specifies the condition that the signal is maximized when the RF field is unaffected by the sample.

To account for the full volume of metal in which the nuclear spins are excited, the areas of each triangle in the surface mesh, A_q, as well as skin effects must be considered. The latter are incorporated by calculating the decay of the RF signal as a function of the depth, γ, into the conducting metal surface, leading to

$$\omega_q(\gamma) = \omega_q(0) \exp\left(-\frac{\gamma}{\delta}\right), \tag{8}$$

where a skin depth $\delta = 10.4\ \mu$m was employed to match the experimental conditions used here.

By combining Eqs. (7) and (8), an expression for the full MR signal is obtained:

$$F_q = A_q \int_0^\infty \omega_q(\gamma) \sin\left(\omega_q(\gamma)\tau\right) d\gamma. \tag{9}$$

which evaluates exactly to,

$$F_q = \frac{A_q \delta}{\tau}\left[1 - \cos\left(\omega_q(0)\tau\right)\right] \tag{10}$$

This integral was evaluated numerically for each surface triangle. To account for the overlap of the regions near the edges of the metal, the integrals for each triangle were truncated at $\gamma = r_{\text{edge}}$, where r_{edge} is the distance from the center of each triangle to the closest edge of the electrode.

To mimic the imaging experiments, a 2D histogram was built and the F_q values binned depending on their spatial locations relative to the face of the metal.

2.2.2. Susceptibility Calculations

Magnetic field maps were calculated using the FFT method described in Refs 34 and 35. The method takes as input a 3D grid of susceptibility values representing the system to be modeled and uses 3D Fourier transforms of this distribution to efficiently calculate the modifications that are made to the local magnetic field at each position due to susceptibility effects. The simulation cell consisted of 512^3 points representing a cube with 12.8 mm sides. A cuboid in the middle

of the cell measuring 3 x 0.375 x 10 mm (in the x, y, and z directions, respectively, with B_0 aligned along z) corresponded to the lithium metal, and was assigned a volume susceptibility of $\chi_{\text{vol}}^{\text{Li}} = 24.1 \times 10^{-6}$ [36, 37] in SI units, while the rest of the cell was modeled as a vacuum with $\chi_{\text{vol}} = 0$.

The calculation yields the susceptibility-corrected field at each point in the simulation cell, H_0^{eff}. To match the experimental chemical shifts, the Knight shift must also be accounted for. Its contribution is defined as a constant offset, K, that directly scales the resonance frequency, $H_0^{\text{exp}} = (1 + K)H_0^{\text{eff}}$, where $K = 0.0261\%$ for ^{7}Li metal [2, 38].

The NMR spectrum was reproduced from the susceptibility results by generating a separate histogram of the chemical shifts for the surface sites on each side of the metal. Artificial line broadening of 2 ppm was used to smoothen discretization artifacts and to aid the comparison with the experimental spectra.

3. Results

Numerical calculations were performed on a Li metal slab at different relative orientations to the RF field in order to explore the angular dependence of the total RF field strength. Plots of the numerically calculated total field, H^{tot} at locations on the surface of the Li metal (Figure 2) show that it has a strong dependence on ϕ_{RF}. As a general rule, the faces of the metal that are perpendicular to the propagation direction of the RF field experience a significantly diminished H^{tot} field. This reduction can be thought of as being caused by the induced eddy currents, which, according to Lenz's law, produce a magnetic field opposing that of the RF field. As the eddy currents circulate perpendicular to the the RF field direction, their effect is much greater on the faces of the metal that are also perpendicular to the RF field direction.

The spatial variations in the field, displayed in Figure 2, give rise to the variations in the detected MR signal from the metal surface. As detailed in the methods section, the MR signal can be simulated from the x and y components of the H^{tot} field map and converted into a histogram that shows the xy distribution of MR signal, facilitating a direct comparison with 2D MRI images (Figure 3). The experimental images are in remarkable agreement with the simulated results and both inherit recognizable features from the field maps in Figure 2. At $\phi_{\text{RF}} = 0°$, the major, ac faces of the metal strip are uniformly excited, while the minor, bc faces show little or no excitation (see Figure 1 for edge/face labels). As the field is rotated the signal increases at the bc faces until, at $\phi_{\text{RF}} = 90°$, it becomes the main contribution to the overall signal. The signal due to the ab faces is too small and distributed over a large area so is not immediately apparent in the MR images or the calculation results.

There are minor discrepancies between the simulated and experimental results at the corners of the metal strip when $\phi_{\text{RF}} = 60°$ and $90°$. Such discrepancies are expected, because the corners represent numerically challenging regions, and the metal plate used in the experiment does not have perfectly sharp edges. There is also poor agreement in the relative intensities of the simu-

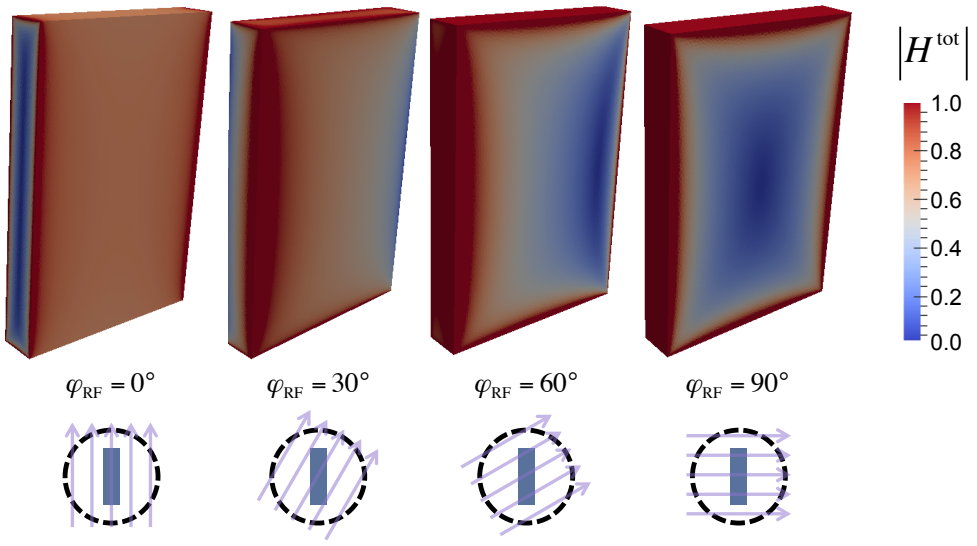

Figure 2: Plots of the calculated field at the surface of the metal when the direction of the applied field is rotated with respect to the metal strip face at ϕ_{RF}= 0, 30, 60, 90°. Bottom: Depiction of the relative orientations of the metal strip face and the direction of field propagation.

lated images for $\phi_{RF} = 60°$ and 90°, which could possibly be due to an issue with the exact pulse calibration.

The excellent overall agreement between the simulated images and those obtained experimentally validates the calculation method and the approximations used. It also confirms the importance of aligning the sample to $\phi_{RF} = 0°$ in order to acquire artifact-free MR images of bulk metals. More significantly, the spatial variation in H^{tot} will also enable the use of nutation experiments that can actively select different faces of a metal strip or, facilitated by numerical calculations, specific locations on the surface of any arbitrarily shaped conductor (on distance scales much larger than the skin-depth). This approach has great potential in application to battery systems, where it may be possible to use nutation experiments to select only the active faces of a metal electrode, giving some degree of spatial selectivity without requiring time-intensive imaging techniques.

The dependence on the relative RF field orientation also has far reaching consequences for NMR spectroscopy experiments performed on samples that are good conductors, and particularly for the quantification of the NMR signal. As expected, 1D NMR spectra of the ^{7}Li metal strip at different field orientations (Figure 4(a)), show a strong dependence of the total signal intensity on ϕ_{RF}. These changes follow directly from the results of Figure 3, but the relative signal contributions will also depend on sample orientation. One clue that this is indeed observed, is in the apparent emergence of the peak at ≈265 ppm when $\phi_{RF} = 90°$. The susceptibility calculations (Figure 4(b)) show that the ^{7}Li nuclei on the top and bottom (*ab*, in green) faces of the metal are

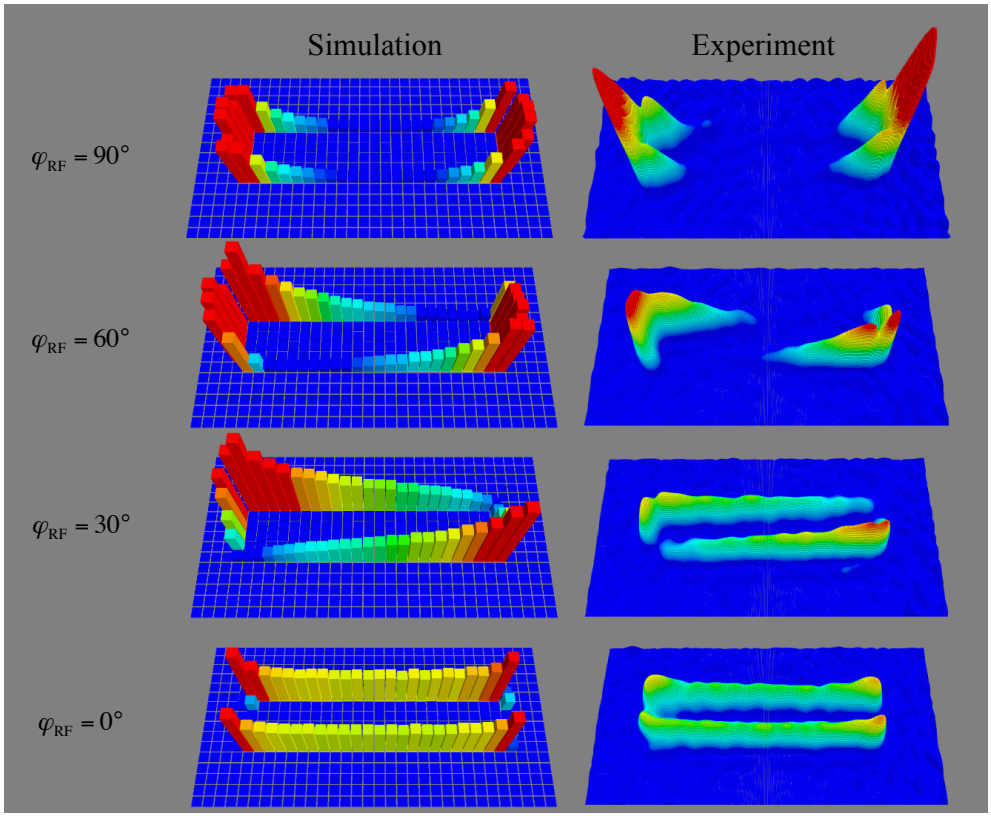

Figure 3: Results from simulations (left) and experiment (right) corresponding, from bottom to top, to ϕ_{RF}= $0, 30, 60, 90°$. The plots within each series are drawn at the same scale. Each experimental image displays a region of approximately 4.5 x 1.5 mm in the directions parallel and perpendicular to the major face of the metal, respectively.

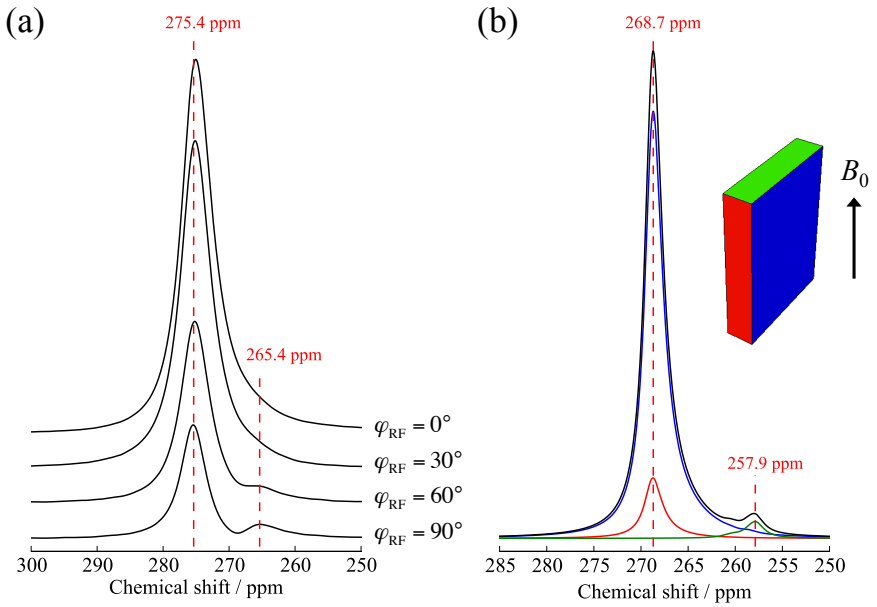

Figure 4: (a) Experimental NMR spectra of the Li-metal phantom at each orientation, (b) simulated NMR spectrum from the susceptibility calculations, with line colors corresponding to the faces illustrated in the accompanying schematic, while the black line is the sum.

shifted upfield with respect to the nuclei on the other faces, solely due to susceptibility effects. Meanwhile, the field calculations show that H^{tot} on the *ab* faces has a minimal dependence on ϕ_{RF} (increasing only slightly from $\phi_{\text{RF}} = 0°$ to $\phi_{\text{RF}} = 90°$) and so the overall signal from these faces should stay constant with ϕ_{RF}, while the contributions from the other faces vary strongly. Indeed, this is precisely what is observed in the experimental spectra; the intensity of the upfield peak is almost unchanged throughout the series (it is still observed as a shoulder on the larger peak at $\phi_{\text{RF}} = 0°$) while the intensity of the peak at ≈275 ppm reduces on moving from $\phi_{\text{RF}} = 0°$ to $\phi_{\text{RF}} = 90°$.

It is noted that the shifts of the calculated peaks in Figure 4(b) do not match exactly with the experimental values in Figure 4(a), although the separation of the peaks, ≈10 ppm, is reproduced. The calculation depends only on the constants for the susceptibility and Knight shift of Li metal, but assumes a perfect cuboid of the metal ($\chi = \chi^{\text{Li}}_{\text{vol}}$) in a vacuum ($\chi = 0$). There is some variation in the literature regarding the exact values of K and $\chi^{\text{Li}}_{\text{vol}}$ which may contribute to the discrepancy in the shifts. Any diamagnetic chemical impurities on the surface of the Li metal, formed due to reactions with air, or leftover from the preparation technique (the surface of the metal can retain traces of a residue left over from manufacturing, some of which may remain even after cleaning), will also accentuate the shift difference between the faces and impact the shifts.

Despite the slight differences in the chemical shift values, the behavior of the extra peak

upon changes to ϕ_{RF}, and its upfield shift, support its assignment to Li sites on the *ab* faces of the metal. Similar assignments have also been made in battery systems, where Li-microstructures growing perpendicular to the surface of the electrode have been shown to display a significant shift away from the bulk metal peak [19, 21], and where orientation-dependent bulk magnetic susceptibility effects have been explored [39]. In non-conducting samples, the latter leads to a broadening of the spectrum as the shifts vary continuously from one part of the sample to another. In conductors, however, the skin depth effects ensure that only surface sites are probed, hence discrete sets of shifts can be observed without the associated broadening. It is possible that by manipulating the shape of the electrodes, controlling ϕ_{RF}, and explicitly considering the materials surrounding the electrodes, the resolution between these sites could be increased so that certain faces of an electrode could be preferentially probed using MR techniques. The susceptibility calculations used here [34] are fully flexible and could be adapted to aid in the design of such systems.

4. Conclusions

The dependence of the RF field on the orientation of bulk metal plates placed within the RF coil has been investigated both experimentally and theoretically. This dependence was explored using numerical field calculations that have been validated by direct comparison to experimental MRI results. The results show that not all of the faces of a conducting cuboid can be uniformly excited at any orientation, with the faces whose normals are parallel to the field direction experiencing greatly reduced fields. Furthermore, edges and corners typically produce larger signals in any orientation. Given the calculated RF fields and susceptibility shifts, the NMR spectra of a metal plate at any orientation can be fully reconstructed. It is envisaged that the insights into the spatial variations of the field offered by the calculations will enable quantitative surface NMR and MRI studies of bulk metals. Furthermore, through a combination of sample shape and orientation, studies directed at diagnosing surface roughness or microstructure growth could be performed. This approach should be particularly useful for NMR and MRI of battery systems or other electrochemical devices. In combination with susceptibility calculations, this procedure allows the NMR spectra of conductors to be fully described.

Acknowledgements

This work is part of the NECCES (Northeastern Center for Chemical Energy Storage), an Energy Frontier Research Center funded by the U.S. Department of Energy (DOE), Office of Basic Energy Sciences under Award Number DE-SC0001294 (in situ methodology), and was funded by matching support from NYSTAR-NYSDED, and by the New York State Energy Research Development Authority (NYSERDA) (H.J.C.). The work of L.G. and A.K. was supported by the Applied Mathematical Sciences Program of the U.S. Department of Energy under Contract

DEFGO288ER25053 and by the Office of the Assistant Secretary of Defense for Research and Engineering and AFOSR under NSSEFF Program Award FA9550-10-1-0180.

References

References

[1] J. D. Jackson, Classical Electrodynamimcs, 3rd Edition, John Wiley & Sons Inc, 1990.

[2] H. S. Gutowsky, B. R. McGarvey, Nuclear magnetic resonance in metals. i. broadening of absorption lines by Spin-Lattice interactions, J. Chem. Phys. 20 (9) (1952) 1472–1477.

[3] B. R. McGarvey, H. S. Gutowsky, Nuclear magnetic resonance in metals. II. temperature dependence of the resonance shifts, J. Chem. Phys. 21 (12) (2004) 2114–2119.

[4] A. Narath, H. T. Weaver, Effects of electron-electron interactions on nuclear spin-lattice relaxation rates and knight shifts in alkali and noble metals, Phys. Rev. 175 (2) (1968) 373–382.

[5] S. Abati, E. Borchi, P. C. Coppi, S. De Gennaro, Knight shifts in solid noble metals, Phys. Lett. A 46 (4) (1973) 255–256.

[6] J. J. van der Klink, H. B. Brom, NMR in metals, metal particles and metal cluster compounds, Prog. Nucl. Magn. Reson. Spectrosc. 36 (2) (2000) 89–201.

[7] E. R. Andrew, W. S. Hinshaw, R. S. Tiffen, NMR in rapidly rotated metallic aluminium and cadmium, J. Magn. Reson. 15 (2) (1974) 191–195.

[8] E. R. Andrew, J. L. Corolan, P. J. Randall, More presice knight shift measurements: Application to copper, Phys. Lett. A 35 (6) (1971) 435–436.

[9] U. El-Hanany, M. Shaham, D. Zamir, NMR study of the electronic structure of solid and liquid silver metal, Phys. Rev. B 10 (6) (1974) 2343–2348.

[10] A. Narath, Nuclear magnetic resonance and relaxation of au197 in gold metal and ag109 in gold-silver alloys, Phys. Rev. 163 (2) (1967) 232–237.

[11] A. Narath, Nuclear magnetic resonance and relaxation in iridium metal: The nuclear magnetic dipole moments of ir191 and ir193, Phys. Rev. 165 (2) (1968) 506–511.

[12] G. A. Matzkanin, J. J. Spokas, C. H. Sowers, D. O. Van Ostenburg, H. G. Hoeve, Solute knight shift and nuclear spin-lattice relaxation in ag- and au-base solid solutions, Phys. Rev. 181 (2) (1969) 559–563.

[13] A. Narath, H. T. Weaver, Nuclear magnetic resonance and relaxation of 195Pt in platinum-palladium alloys, Solid State Commun. 6 (6) (1968) 413–415.

[14] N. Bloembergen, T. J. Rowland, On the nuclear magnetic resonance in metals and alloys, Acta metall. 1 (6) (1953) 731–746.

[15] R. J. Snodgrass, Silver nuclear magnetic resonance in silver-transition-metal solid solutions, Phys. Rev. B 3 (11) (1971) 3738–3747.

[16] A. W. Overhauser, Polarization of nuclei in metals, Phys. Rev. 92 (2) (1953) 411–415.

[17] N. Bloembergen, On the magnetic resonance absorption in conductors, J. Appl. Phys. 23 (12) (1952) 1383–1389.

[18] B. A. Hargreaves, P. W. Worters, K. B. Pauly, J. M. Pauly, K. M. Koch, G. E. Gold, Metal-induced artifacts in MRI, Am. J. Roentgenol 197 (3) (2011) 547–555.

[19] R. Bhattacharyya, B. Key, H. Chen, A. S. Best, A. F. Hollenkamp, C. P. Grey, In situ NMR observation of the formation of metallic lithium microstructures in lithium batteries, Nature Mater. 9 (6) (2010) 504–510.

[20] F. Blanc, M. Leskes, C. P. Grey, In situ solid-state NMR spectroscopy of electrochemical cells: Batteries, supercapacitors, and fuel cells, Acc. Chem. Res. 46 (9) (2013) 1952–1963.

[21] S. Chandrashekar, N. M. Trease, H. J. Chang, L.-S. Du, C. P. Grey, A. Jerschow, 7Li MRI of li batteries reveals location of microstructural lithium, Nature Mater. 11 (4) (2012) 311–315.

[22] M. Klett, M. Giesecke, A. Nyman, F. Hallberg, R. W. Lindström, G. Lindbergh, I. Furó, Quantifying mass transport during polarization in a li ion battery electrolyte by in situ 7Li NMR imaging, J. Am. Chem. Soc. 134 (36) (2012) 14654–14657.

[23] M. M. Britton, P. M. Bayley, P. C. Howlett, A. J. Davenport, M. Forsyth, In situ, real-time visualization of electrochemistry using magnetic resonance imaging, J. Phys. Chem. Lett. (2013) 3019–3023.

[24] J. A. Tang, G. Zhong, S. Dugar, J. A. Kitchen, Y. Yang, R. Fu, Solid-state STRAFI NMR probe for material imaging of quadrupolar nuclei, J. Magn. Reson. 225 (2012) 93–101.

[25] A. Maue, On the formulation of a general scattering problem by means of an integral equation, Z. Phys 126 (7) (1949) 601–618.

[26] M. Taskinen, P. Yla-Oijala, Current and charge integral equation formulation, IEEE Trans. Antennas Propagat. 54 (1) (2006) 58–67. doi:10.1109/TAP.2005.861580.

[27] F. Vico, Z. Gimbutas, L. Greengard, M. Ferrando-Bataller, Overcoming low-frequency breakdown of the magnetic field integral equation, IEEE Trans. Antennas and Propagation 61 (2013) 1285–1290.

[28] D. Colton, R. Kress, Integral Equation Methods in Scattering Theory, John Wiley & Sons Inc, 1983.

[29] Y. Saad, M. H. Schultz, GMRES: A generalized minimal residual algorithm for solving nonsymmetric linear systems, SIAM Journal on scientific and statistical computing 7 (3) (1986) 856–869.

[30] H. Cheng, W. Y. Crutchfield, Z. Gimbutas, L. F. Greengard, J. F. Ethridge, J. Huang, V. Rokhlin, N. Yarvin, J. Zhao, A wideband fast multipole method for the Helmholtz equation in three dimensions, Journal of Computational Physics 216 (1) (2006) 300–325.

[31] L. Greengard, Z. Gimbutas, fmmlib3d Fast Multipole subroutine library (2012).
URL http://www.cims.nyu.edu/cmcl/fmm3dlib/fmm3dlib.html

[32] C. Geuzaine, J.-F. Remacle, Gmsh: A 3-d finite element mesh generator with built-in pre-and post-processing facilities, International Journal for Numerical Methods in Engineering 79 (11) (2009) 1309–1331.

[33] D. I. Hoult, The principle of reciprocity in signal strength calculations—A mathematical guide, Concepts Magn. Reson. 12 (4) (2000) 173–187.

[34] R. Salomir, B. D. de Senneville, C. T. Moonen, A fast calculation method for magnetic field inhomogeneity due to an arbitrary distribution of bulk susceptibility, Concepts Magn. Reson. 19B (1) (2003) 26–34.

[35] J. Marques, R. Bowtell, Application of a fourier-based method for rapid calculation of field inhomogeneity due to spatial variation of magnetic susceptibility, Concepts Magn. Reson. B 25B (1) (2005) 65–78.

[36] D. Gugan, Martensitic transformation of lithium: Magnetic susceptibility measurements, Phys. Rev. B 56 (13) (1997) 7759.

[37] F. T. Hedgcock, Magnetic susceptibility of the two phases of lithium at low temperatures, Phys. Rev. Lett. 5 (9) (1960) 420–423.

[38] T. J. Rowland, Nuclear magnetic resonance in metals, Prog. Mater. Sci. 9 (1) (1961) 3–91.

[39] L. Zhou, M. Leskes, A. J. Ilott, N. M. Trease, C. P. Grey, Paramagnetic electrodes and bulk magnetic susceptibility effects in the in situ NMR studies of batteries: Application to Li1.08Mn1.92O4 spinels, J. Magn. Reson. 234 (2013) 44–57.